nature catalysis

Article

https://doi.org/10.1038/s41929-023-01020-4

Selective electrochemical synthesis of urea from nitrate and CO_2 via relay catalysis on hybrid catalysts

Received: 3 November 2022

Accepted: 1 August 2023

Published online: 11 September 2023

Check for updates

Yuting Luo[1,6], Ke Xie[1,6], Pengfei Ou[1,6], Chayse Lavallais[2,6], Tao Peng[1,5], Zhu Chen[1], Zhiyuan Zhang[3], Ning Wang[1], Xiao-Yan Li[1], Ivan Grigioni[1], Bilu Liu[3], David Sinton[4], Jennifer B. Dunn[2] ✉ & Edward H. Sargent[1] ✉

The nitrogen cycle needed for scaled agriculture relies on energy- and carbon-intensive processes and generates nitrate-containing wastewater. Here we focus on an alternative approach—the electrified co-electrolysis of nitrate and CO_2 to synthesize urea. When this is applied to industrial wastewater or agricultural runoff, the approach has the potential to enable low-carbon-intensity urea production while simultaneously providing wastewater denitrification. We report a strategy that increases selectivity to urea using a hybrid catalyst: two classes of site independently stabilize the key intermediates needed in urea formation, $*CO_2NO_2$ and $*COOHNH_2$, via a relay catalysis mechanism. A Faradaic efficiency of 75% at wastewater-level nitrate concentrations (1,000 ppm NO_3^- [N]) is achieved on Zn/Cu catalysts. The resultant catalysts show a urea production rate of 16 μmol h^{-1} cm^{-2}. Life-cycle assessment indicates greenhouse gas emissions of 0.28 kg CO_2e per kg urea for the electrochemical route, compared to 1.8 kg CO_2e kg^{-1} for the present-day route.

During 2020, anthropogenically activated nitrogen reached ~150 million metric tonnes (Mt), 2.5 times greater than the production of the natural baseline[1] (60 Mt). Anthropogenic nitrogen activation starts by converting dinitrogen (N_2) and steam-methane-reformed hydrogen (H_2) to ammonia via the Haber–Bosch process at elevated temperatures (>350 °C) and very high pressures (>10 MPa)[2]. Ammonia is then further processed to nitrogen-containing chemicals (Fig. 1a)[3–6], including urea-based fertilizer (for which fully 47% of ammonia production is employed), with urea having an annual production of 180 Mt. This accounts for 1% of global annual energy consumption and emits net CO_2 of over 200 Mt each year.

Nitrogen-containing waste generated by human activities must be deactivated to N_2 via biological[7] (wastewater) or thermocatalytic[8] (waste gas) processes before it is discharged, and this contributes a further 2% of energy consumption and 0.5% of global greenhouse gas (GHG) emissions[7]. The nitrogen activation/deactivation cycle (Fig. 1b) is energy-intensive as a result of the reliance on an inert mediator (N ≡ N bond, 941 kJ mol^{-1}).

The electrochemical conversion of activated-nitrogen-containing wastes (nitrate, nitrile, NO_x) offers an alternative nitrogen cycle, one that can potentially be implemented under mild conditions (Fig. 1c): nitrate to urea achieved by co-feeding CO_2 (refs. 5,9–15). Nitrate (NO_3^-)

[1]Department of Electrical and Computer Engineering, University of Toronto, Toronto, Ontario, Canada. [2]Department of Chemical and Biological Engineering, Northwestern University, Evanston, IL, USA. [3]Shenzhen Geim Graphene Center, Tsinghua-Berkeley Shenzhen Institute & Institute of Materials Research, Shenzhen International Graduate School, Tsinghua University, Shenzhen, P. R. China. [4]Department of Mechanical and Industrial Engineering, University of Toronto, Toronto, Ontario, Canada. [5]Present address: Beijing Huairou Laboratory, Beijing, China. [6]These authors contributed equally to this work: Yuting Luo, Ke Xie, Pengfei Ou, Chayse Lavallais. ✉e-mail: jennifer.dunn1@northwestern.edu; ted.sargent@utoronto.ca

https://doi.org/10.1038/s41929-023-01020-4

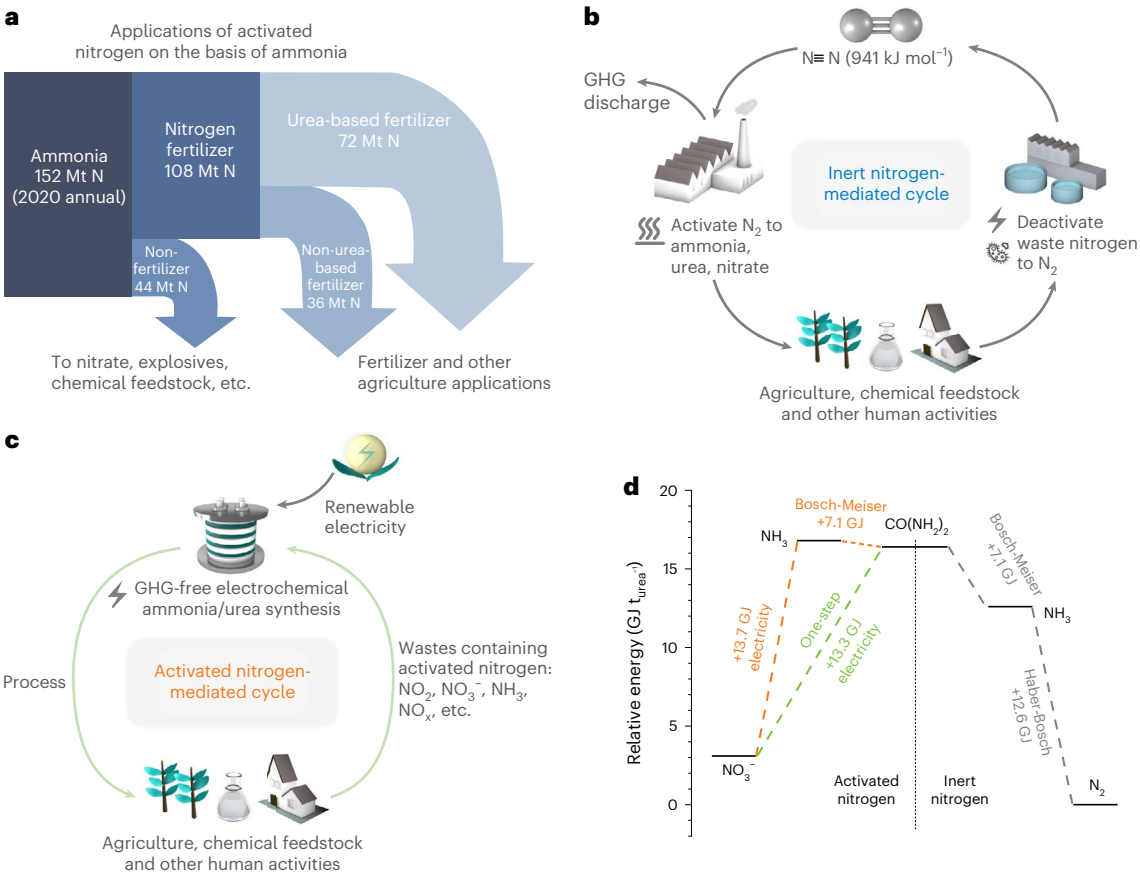

Fig. 1 | Nitrogen cycles and their energetics. a, Present-day ammonia and urea volumes and uses. All data are in million metric tonnes of nitrogen (Mt N) per year using production data for 2020[6]. **b**, The existing inert-nitrogen (N_2) mediated cycle. **c**, The activated-nitrogen cycle explored herein, one based on nitrate, NO_3^-. **d**, Energy requirements for one-step (green) and two-step (orange) urea electrosynthesis processes and the energy requirements for the industrial production of urea (grey).

from industrial wastewater and agricultural runoff[16,17] can be converted to urea via a two-step approach:

$$NO_3^- + 2H_2O \rightarrow NH_3 + 2O_2 + OH^-$$
$$E^0 = 0.53\,V\,(13.7\,GJ/\,metric\,tonne\,urea) \quad (1)$$

$$2NH_3 + CO_2 \rightarrow CO(NH_2)_2 + H_2O$$
$$Bosch-Meiser\,process\,(practical):\ 7.1\,GJ/\,metric\,tonne\,urea \quad (2)$$

or a one-step approach:

$$CO_2 + 2NO_3^- + 3H_2O \rightarrow CO(NH_2)_2 + 4O_2 + 2OH^-$$
$$E^0 = 0.51\,V\,(13.3\,GJ/\,metric\,tonne\,urea) \quad (3)$$

As shown in Fig. 1d, the one-step electrosynthesis of urea from NO_3^- and CO_2 could be of interest once it can be achieved at modest overpotentials, offering an advantage in overall energetics compared to the two-step and industrial approaches[18,19] (Supplementary Note 1 and Supplementary Tables 1 and 2).

Achieving this shift to a new and potentially more efficient nitrogen cycle will require the development of electrocatalysts with high urea selectivity via the co-electrolysis of NO_3^- and CO_2. The catalysts should provide C–N coupling while minimizing side reactions from nitrate (nitrate reduction reaction, NO_3RR), CO_2 (carbon dioxide reduction reaction, CO_2RR) and H_2O (hydrogen evolution reaction, HER). Previous studies have reported catalysts capable of producing urea from NO_3^- and CO_2 (Supplementary Table 3)[5,11,20,21], but these have been limited to <20% Faradaic efficiency (FE) when realistic nitrate concentrations are used (such as 200 ppm), as HER becomes dominant. NO_3^- and CO_2 must adsorb simultaneously onto the catalyst for C–N coupling to be achieved, but the competing single-precursor reductions—NO_3RR to N_2 or NH_3 (ref. 22) and CO_2RR to CO (ref. 21)—then take over, competing against the desired high selectivity to a single desired product, urea.

Synthesizing urea from NO_3^- by co-feeding CO_2 is a multistep reaction involving 16 electrons being transferred for each urea molecule. The first C–N bond formation (intermediate $*CO_2NO_2$) and the protonation of $*CO_2NH_2$ (intermediate $*COOHNH_2$) are the two key steps of urea formation[5]. The relative reaction energies of the steps are correlated when described via scaling relations, suggesting instead the need for independent tailoring of the reaction energy for distinct sites, as well as a handoff of key intermediates among sites, to circumvent the scaling relations.

In this Article we report a strategy that increases the selectivity to urea by using a hybrid catalyst. When we apply and optimize the Zn/Cu hybrid catalyst, we achieve FEs of 75% at 1,000 ppm NO_3^- [N]. Experiments and density functional theory (DFT) calculations reveal a relay catalysis mechanism in which $*CO_2NO_2$—the key intermediate for C–N coupling—preferentially forms on Zn sites, and the ensuing protonation step to form $*COOHNH_2$ benefits from a lowered reaction energy on nearby Cu sites. The resulting catalyst shows a urea production rate of 16 μmol h^{-1} cm^{-2} (60 mmol h^{-1} g_{cat}^{-1}) at −0.8 V versus reversible hydrogen

https://doi.org/10.1038/s41929-023-01020-4

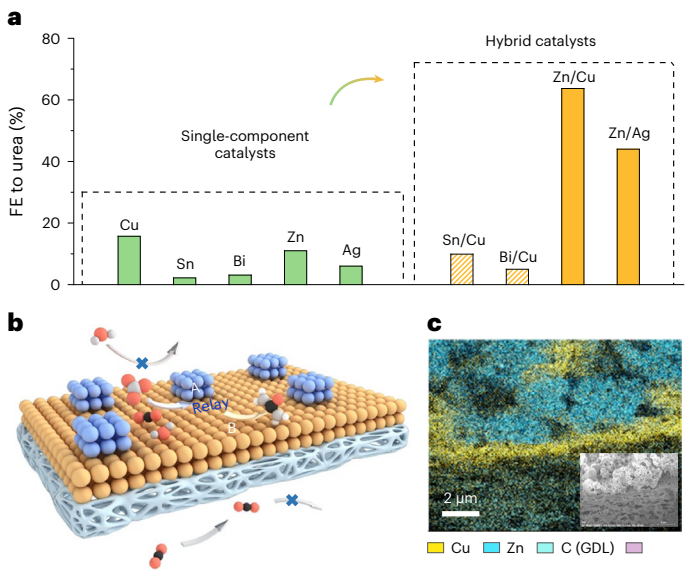

Fig. 2 | Screening of single-component and hybrid catalysts. a, Screening of single-component catalysts and hybrid catalysts. All the catalysts are compared at a potential of −0.6 V versus RHE in electrolytes containing KNO_3 (500 ppm NO_3^- [N]) and $KHCO_3$ (0.1 M). The solid orange columns indicate hybrid catalysts that increase the selectivity to urea compared to their single-component counterparts; the hashed columns indicate catalysts not increasing the selectivity to urea. **b**, A hybrid catalyst, where one component (blue) lowers the reaction energy of the C–N bond-formation step, and a second component (orange) reduces the reaction energy of the protonation step needed to produce urea. Red, dark, grey and white denote O, C, N and H. **c**, EDS mapping of a Zn/Cu hybrid catalyst.

electrode (RHE) in 1,000 ppm NO_3^- [N]. A life cycle assessment indicates that, when CO_2 embodied in the urea is emitted at the end of life, GHG emissions are 0.28 kg CO_2e kg^{-1} for the electrochemical route compared to 1.8 kg CO_2e kg^{-1} for the conventional route.

Results

Design of hybrid catalysts

We first screened single-component metals known to prefer CO_2RR and NO_3RR over HER. We found that Cu, Sn, Bi, Zn and Ag enable modest levels of urea synthesis, with FEs to urea of <20% at 500 ppm NO_3^- [N] (Fig. 2a) at −0.6 V versus RHE (details are provided in the Methods). To investigate their low selectivity to urea, we used DFT calculations to analyse the reaction pathway for the co-electrolysis of NO_3^- and CO_2 on some of the single-component metals (Supplementary Fig. 1). The adsorption of $*NO_2$ is energetically favoured on these metal surfaces, then followed by either a first C–N bond-formation step ($*CO_2NO_2$) or the reduction of $*NO_2$ (ref. 5). The reaction energy for such a C–N bond-formation step is much smaller on a Zn surface than on Cu or Ag. The reaction energy for the protonation step ($*COOHNH_2$), however, is smaller on Cu or Ag surfaces than it is on Zn. This explains the low urea FEs on single-component metals and offers an explanation for the higher performance of multi-component catalysts.

This motivated us to explore hybrid catalysts, where the first class of sites would lower the barrier energy associated with the C–N bond-formation step, and a second would reduce that for the protonation step to produce urea (Fig. 2b). We then screened hybrid catalysts composed of pairs of the same list of metals (Fig. 2a). Among these, Zn/Cu (64%) and Zn/Ag (44%) showed striking improvements compared to single-component catalysts.

We then sought to characterize the distribution of Cu and Zn on a gas-diffusion layer (GDL), with a portion of Cu (Fig. 2c and Supplementary Figs. 2–4) readily accessible to the reactants and intermediates in the liquid phase. The exposed Cu was achieved by spray-coating an incomplete layer of Zn on top of the Cu layer. As seen in X-ray diffraction (XRD) and high-resolution transmission electron microscopy (HR-TEM) investigations, the Zn/Cu hybrid catalysts are based on metallic phases with predominant crystalline facets Cu(111), Cu(200), Zn(002) and Zn(101) (Supplementary Figs. 5 and 6).

Steering selectivity to urea on Zn/Cu catalysts

We evaluated the urea electrosynthesis performance in the electrolytes containing KNO_3 (500 ppm NO_3^- [N]) and $KHCO_3$ (0.1 M), saturated by CO_2. We fed CO_2 into the electrochemical system from a GDL (Supplementary Fig. 7). To quantify urea production, we used UV–vis absorption spectrophotometry, ^{14}N NMR and isotope ^{15}N NMR (Fig. 3a and Supplementary Figs. 8–10). The best hybrid catalysts exhibit urea FEs of 64 ± 3% (Fig. 3a), higher than those of single-component Cu and Zn (FEs of <15%; Fig. 3a). Controls (Supplementary Fig. 11) indicate the need for electrons (e^-), NO_3^- in the electrolyte, and gaseous CO_2.

We then investigated C–N coupling preference on Zn, Cu and Zn/Cu hybrid catalysts by comparing their urea FEs relative to other reactions. The ratios between $FE_{C-N\text{-}coupling}$ and $FE_{non\text{-}C-N\text{-}coupling}$ indicate selectivity to C–N coupling compared to non-C–N-coupling reactions (Fig. 3b). HER and CO_2RR dominate on single-component Zn and Cu catalysts. CO_2 is mainly converted to formate on the Zn catalyst and C_{2+} products on Cu (Supplementary Fig. 12). By contrast, the Zn/Cu hybrid catalyst exhibits $FE_{CO2RR}/FE_{C-N\text{-}coupling}$ and $FE_{HER}/FE_{C-N\text{-}coupling}$ values of 0.13 and 0.16. Considerable NO_3RR-produced ammonia was detected only on Cu.

We then optimized the Zn and Cu components. X-ray photoelectron spectroscopy (XPS) revealed atomic ratios of Zn:Cu on the surfaces ranging from ~0.4 (0.2 mg cm^{-2} Zn) to 1.4 (0.5 mg cm^{-2} Zn) and 7.8 (2.2 mg cm^{-2} Zn) as the loading of Zn increases (Supplementary Fig. 13). Only NO_3RR products are detected when we employ a pure-Cu catalyst. When we load with even a small amount of Zn (above 0.1 mg cm^{-2}), the Zn/Cu hybrid catalyst shows undetectable NO_3RR products (NH_3, N_2, N_2O, NO and so on; Supplementary Fig. 14). When we increase the Zn loading above 0.8 mg cm^{-2}, we observe much formate, acetic acid and hydrogen (FEs of 5%, 16% and 28%; Supplementary Fig. 15). Formate and hydrogen become the major products (FEs of 18% and 25%) when Zn loading increases to 1 mg cm^{-2}. We did not detect CO on any hybrid catalyst. As a control, we studied $Zn_{50}Cu_{50}$ nanoalloy catalysts (Supplementary Fig. 16), finding that these generate urea with a FE of 26%.

We then further optimized the Zn/Cu hybrid catalyst for selectivity to urea, including varying the electrode configuration (Supplementary Fig. 18). This optimized catalyst, Zn–0.5/Cu, exhibits a potential-dependent product distribution (Fig. 3c), with peak FE at −0.6 V versus RHE, a finding we assign to faster HER kinetics at higher overpotentials (Supplementary Fig. 19b). The competition of HER dominates when the potential is below −0.8 V versus RHE (Supplementary Fig. 19). The urea FEs of Zn/Cu hybrid catalysts are higher than those of previously reported electrocatalysts (Supplementary Table 3).

We studied the catalytic performance of Zn–0.5/Cu at different realistic concentrations of nitrate (Fig. 3d). HER diminishes as the nitrate concentration increases, and CO_2RR does not change much. The urea selectivity varies from 50% at 100 ppm NO_3^- [N] to 75% at 1,000 ppm. We also characterized the performance of Zn–0.5/Cu at higher concentrations of nitrate (Supplementary Fig. 20).

Mechanistic studies

We used in situ infrared reflection–absorption spectroscopy (IRRAS) to detect the intermediates and products across a potential range of +0.3 to −1.2 V versus RHE (Fig. 4a). The infrared bands probed at 1,629 and 1,175 cm^{-1} originate from the bending and rocking modes of $-NH_2$ in urea, respectively[23]. The band at 1,314 cm^{-1} is attributed to the wagging mode of $-NH_2$ (ref. 5). The infrared band at 1,417 cm^{-1}, related to the

https://doi.org/10.1038/s41929-023-01020-4

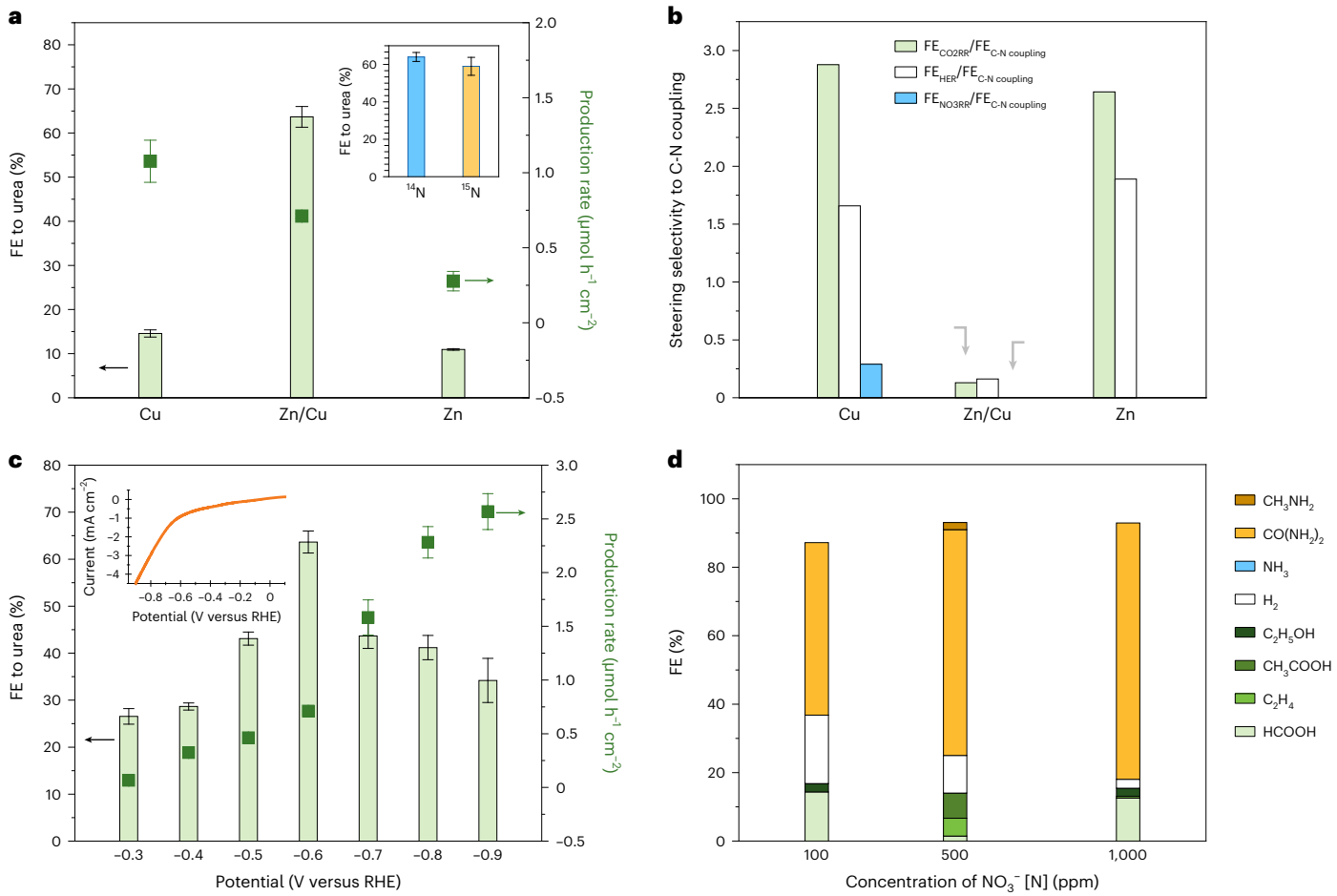

Fig. 3 | Steering selectivity to C–N coupling on Zn/Cu hybrid catalysts. a, FEs to urea on the Zn/Cu hybrid catalyst and single-component counterparts. Inset: detection of urea by ^{14}N and ^{15}N NMR. **b**, Selectivity to C–N coupling and side reactions. Data in **a** and **b** are measured at −0.6 V versus RHE in electrolytes containing KNO_3 (500 ppm NO_3^- [N]) and $KHCO_3$ (0.1 M). **c**,**d**, FE to urea and its production rate on a Zn–0.5/Cu hybrid catalyst under different potentials (**c**) and at different nitrate concentrations (**d**). Inset in **c**: linear sweep voltammetry curve for Zn–0.5/Cu. Data in **c** and **d** are measured in $KHCO_3$ (0.1 M) and KNO_3 with specific concentrations (500 ppm NO_3^- [N] for **c**). Error bars represent s.d. from two independent measurements.

stretching mode of the C–N bond in urea[24], appears when applying negative potentials, but diminishes when elevating the potential to −1.2 V versus RHE. Compared to free urea, the stretching frequency of the C–N bond shifts to a lower wavenumber, indicating that the urea is coordinated with metal ions on the hybrid catalyst through an oxygen atom associated with the C=O group[24]. In situ X-ray absorption spectroscopy shows that the local electronic structure and local geometric structure of the hybrid catalyst are changed negligibly (Supplementary Fig. 21).

In situ IRRAS was performed, and a band at 1,694 cm^{-1} was observed to appear starting at −0.3 V versus RHE, diminishing to near zero at −1.2 V versus RHE, the range over which urea synthesis occurs. This band has previously been assigned to C=O in the $COOHNH_2$ dimer[25], a carbamate that is usually observed at low temperatures[25]. Compared to the free molecule[25], the stretching frequency of the C=O bond shifts to a higher wavenumber, suggesting that the molecule may be coordinated with metal ions on the hybrid catalyst through the hydroxyl oxygen atom of O–C=O. These results attest to the presence of the intermediate $*COOHNH_2$. We also found that an infrared band arose at 1,403 cm^{-1} under potentials between 0 and −1.2 V versus RHE, something we propose is assigned to the OCO vibrational band, consistent with the presence of $*CO_2NH_2$ (ref. 5). These results agree with the picture in which protonation of CO_2NH_2 to $COOHNH_2$ is a key step for urea synthesis.

For comparison, we performed IRRAS on single-component Zn and Cu. On the Zn, a weak band arises at 1,404 cm^{-1} ($*CO_2NH_2$) when the potential is between −0.3 and −1.2 V versus RHE, but there is no band near 1,694 cm^{-1} ($*COOHNH_2$) (Supplementary Fig. 22). The rate-determining step on Zn is therefore suggested to be the protonation of $*CO_2NH_2$ to form $*COOHNH_2$. On the Cu, we did not observe bands near 1,404 cm^{-1} nor 1,694 cm^{-1} (Supplementary Fig. 22). This can be explained if the first C–N bond formation is a rate-determining step on Cu.

We also used in situ surface-enhanced Raman spectroscopy (SERS) to detect intermediates on the Zn/Cu hybrid catalyst (Fig. 4b–d). Ammonium carbamate (NH_2COONH_4, AC) was used as a reference; this consists of $CO_2NH_2^-$ in aqueous solution, together with the ions NH_4^+, HCO_3^- and CO_3^{2-}. The same peak at 334–337 cm^{-1}, the feature assigned to M–$OCONH_2$ ($*CO_2NH_2$), was detected under urea synthesis conditions (Fig. 4b) and in the AC solution (Fig. 4c), but not in $KHCO_3$ solution (Fig. 4d) nor in other control conditions (Supplementary Fig. 23). The $*CO_2NH_2$ signal was observed at ~−0.5 V versus RHE under urea synthesis conditions and −0.3 V in the AC solution. On single-component Cu, we observed only the $*CO_2NH_2$ signal in the AC solution, starting at −0.1 V versus RHE (Supplementary Figs. 24 and 25). These results are in line with the view that Zn may contribute to the formation of the needed $*CO_2NH_2$ intermediate.

DFT calculations were used to further study the functions of Zn and Cu in the hybrid catalysts (Fig. 4e,f). Following the adsorption and reduction of NO_3^- on the Zn surface (step 1), a CO_2 molecule inserts to

https://doi.org/10.1038/s41929-023-01020-4

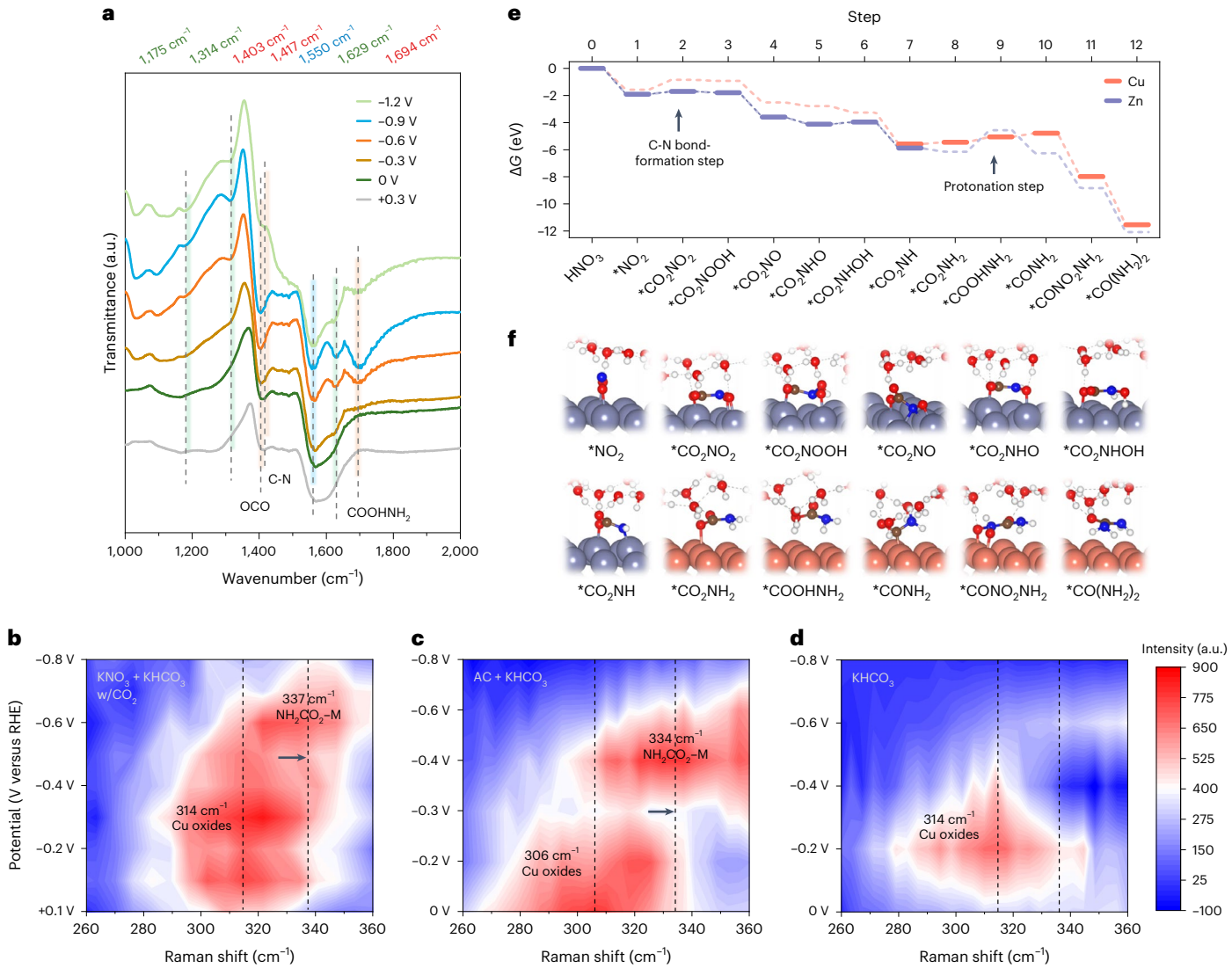

Fig. 4 | Mechanistic study elucidating a chemical picture of relay catalysis. **a**–**d**, In situ IRRAS (**a**) and in situ SERS (**b**–**d**) measurements on Zn/Cu under various potentials versus RHE in electrolytes of 1 M $KHCO_3$ + 1 M KNO_3 (**b**), 0.03 M AC + 0.7 M $KHCO_3$ (**c**) and 1 M $KHCO_3$ (**d**). The arrows indicate the potentials at which the peak of $*CO_2NH_2$ appears. **e**, DFT calculations of the free-energy diagram for the synthesis of urea from NO_3^- and CO_2 (**e**) and corresponding atomic configurations for each step (**f**). Orange, grey, red, blue, brown and white denote Cu, Zn, O, N, C and H, respectively. The Zn surface, after adsorption of a $*NO_2$ (step 1), energetically favours C–N bond formation to form $*CO_2NO_2$ (step 2, insertion of a CO_2 molecule) more than the Cu surface, whereas the latter diminishes the reaction energy for the potential-determining protonation step on Zn (step 9) so as to complete a catalytic loop.

form a C–N bond, with its oxygen atom bonded to another Zn atom to form $*CO_2NO_2$ (step 2). This step is more energetically favourable on the Zn surface than on the Cu (Fig. 4e). The reaction energy for step 9 is higher on the Zn surface (-1.8 eV) than on the Cu surface (-0.5 eV), corresponding to the protonation of $*CO_2NH_2$ to form $*COOHNH_2$ (Fig. 4e), which suggests that the Cu surface is necessary to accomplish a catalytic loop for urea synthesis following a relay catalysis pathway. In this way, the reaction energies for the two steps—the C–N bond-formation step (intermediate $*CO_2NO_2$) and the protonation step (intermediate $*COOHNH_2$)—are independently tuned by the Zn/Cu hybrid catalyst.

Hybrid catalysts composed of two classes of site, where one promotes C–N bond formation and another facilitates protonation, have the potential to circumvent the need to balance the adsorption energies for all the elementary steps using a single catalytic site. The Zn/Cu hybrid catalyst implements a relay catalysis mechanism in which both Zn and Cu sites are catalytically active and provide distinct functions. One-component catalysts typically facilitate either the C–N bond-formation step or the protonation step, but not both. For example, in Cu@Zn core–shell catalysts, the shell Zn is catalytically active, and its electronic structure is tuned by the core Cu to facilitate the C–N bond-formation step[15]. $In(OH)_3$, having {100} facets, also principally improves the C–N bond-formation step[5].

Hybrid catalysts with high production rate

We sought to apply this catalyst design strategy to three-dimensional (3D) hybrid catalysts to achieve a high urea production rate. The 3D Zn/Cu hybrid catalyst (the measured composition is provided in Supplementary Fig. 26) includes both Cu and Zn sites, and energy dispersive spectroscopy (EDS) and HR-TEM (Fig. 5b and 5c) investigations showed that the Zn is distributed uniformly on the Cu. This catalyst leads to an increased current density at 1,000 ppm NO_3^- [N] (Fig. 5c) compared to the reference case Zn–0.5/Cu, while retaining the same high FE to urea (Fig. 5e). The highest partial current density to urea was obtained at −0.8 V versus RHE, with a production rate of 16 μmol h^{-1} cm^{-2} (Fig. 5e) and a mass production rate of 60 mmol h^{-1} g_{cat}^{-1} at a loading of 0.27 mg_{cat} cm^{-2} (Supplementary Fig. 27), a substantial advance (1.5

https://doi.org/10.1038/s41929-023-01020-4

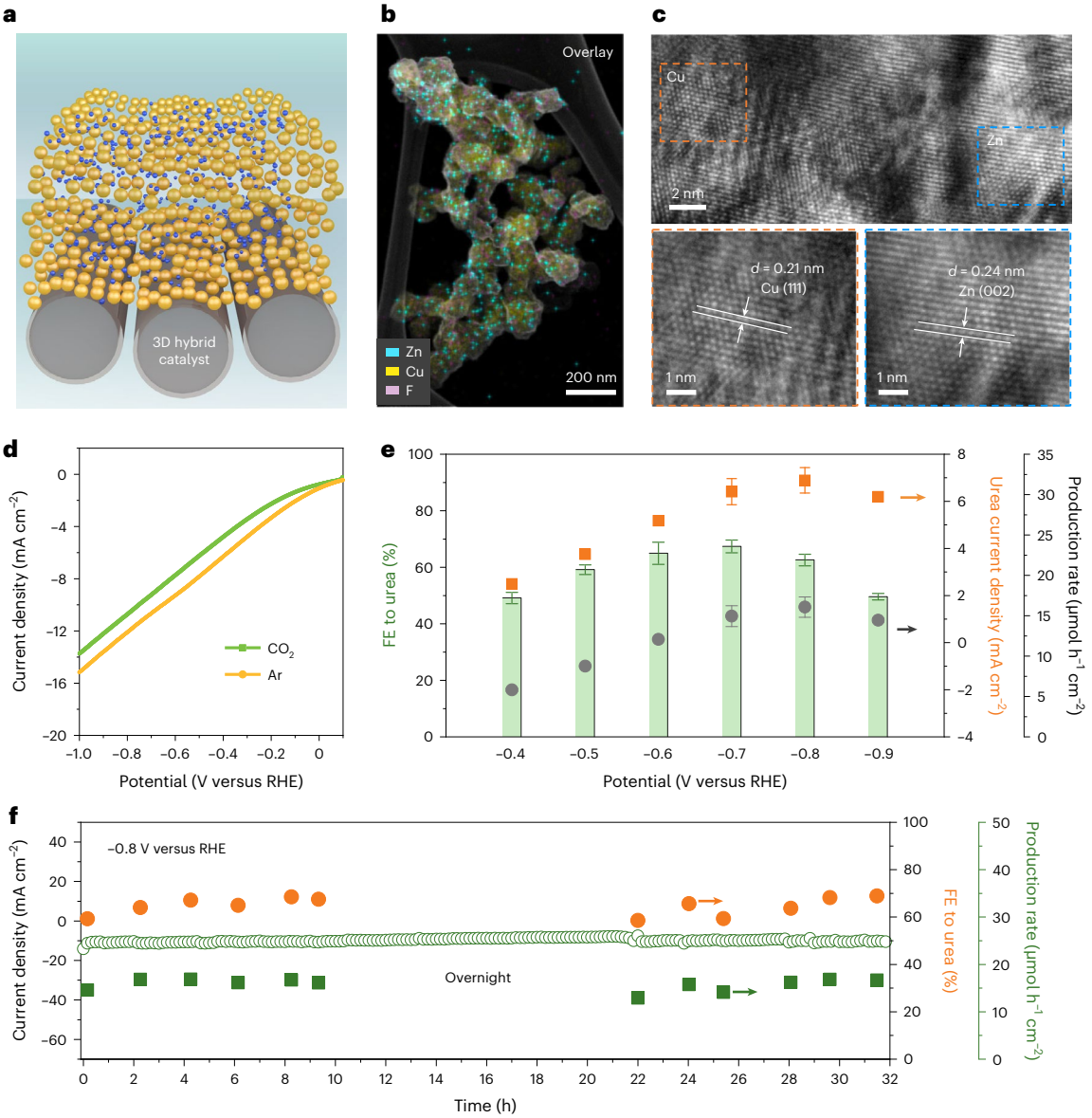

Fig. 5 | 3D hybrid catalyst for urea synthesis at 16 μmol h^{-1} cm^{-2}. a, Scheme of 3D hybrid catalysts on a GDL. Orange and blue denote Cu and Zn. **b**,**c**, Elemental mapping of Cu and Zn, as well as F in Nafion binder (**b**), and HR-TEM images (**c**), revealing the uniform deposition of Zn on Cu. **d**, Linear sweep voltammetry curves while feeding CO_2 or Ar. **e**, FE to urea, its partial current density, and production rate on a 3D Zn/Cu catalyst under different potentials. **f**, Stability test for the 3D Zn/Cu catalyst. Open circles, current density. The experimental tests were conducted in a solution of $KHCO_3$ (0.1 M) and KNO_3 (1,000 ppm NO_3^- [N]). Error bars represent s.d. from three independent measurements.

times improvement in production rate and a tenfold increase in selectivity) compared to previously reported electrocatalysts to urea (Supplementary Table 3).

We evaluated the stability under −0.8 V versus RHE. We found, after operating the catalyst for 32 h at its optimal potential, that the current density was constant to within 5%, and its FE remained within 10% absolute of its initial value. The spent catalyst maintained its morphology and structure (Supplementary Fig. 28).

Life cycle assessment

We performed life cycle assessment (LCA) to compare the cumulative energy demand (CED) and GHG emissions when producing urea conventionally and with the electrochemical technology outlined in this work. The functional unit is 1 kg of 99 wt% urea (Supplementary Figs. 29 and 30). Because the electrosynthesis of urea uses nitrogen from wastewater, we also studied the impact of adding a urea electrosynthesis module in a wastewater treatment plant (WWTP) on its CED and GHG emissions. For this, we used a functional unit of 1 m^3 of treated wastewater (Supplementary Figs. 32 and 33). We considered two different electricity sources: today's US grid (~60% fossil fuel-based power plants) or wind-based renewable. The Methods and Supplementary note 2 present the LCA methodology and data sources.

Traditional urea production through the Bosch–Meiser process uses ammonia from the Haber–Bosch process (Supplementary Fig. 29). This approach was compared with producing urea electrochemically at a WWTP with waste nitrogen equivalent to 1,000 ppm NO_3^- [N] (Supplementary Fig. 30). The CED when producing urea electrochemically is similar to that of conventional production (Supplementary Fig. 34). If the electrical grid provides electricity, producing urea electrochemically is more GHG-intensive than conventional production (Fig. 6a). When grid electricity is used, a large portion of the GHG emissions come from the electricity consumption for the

https://doi.org/10.1038/s41929-023-01020-4

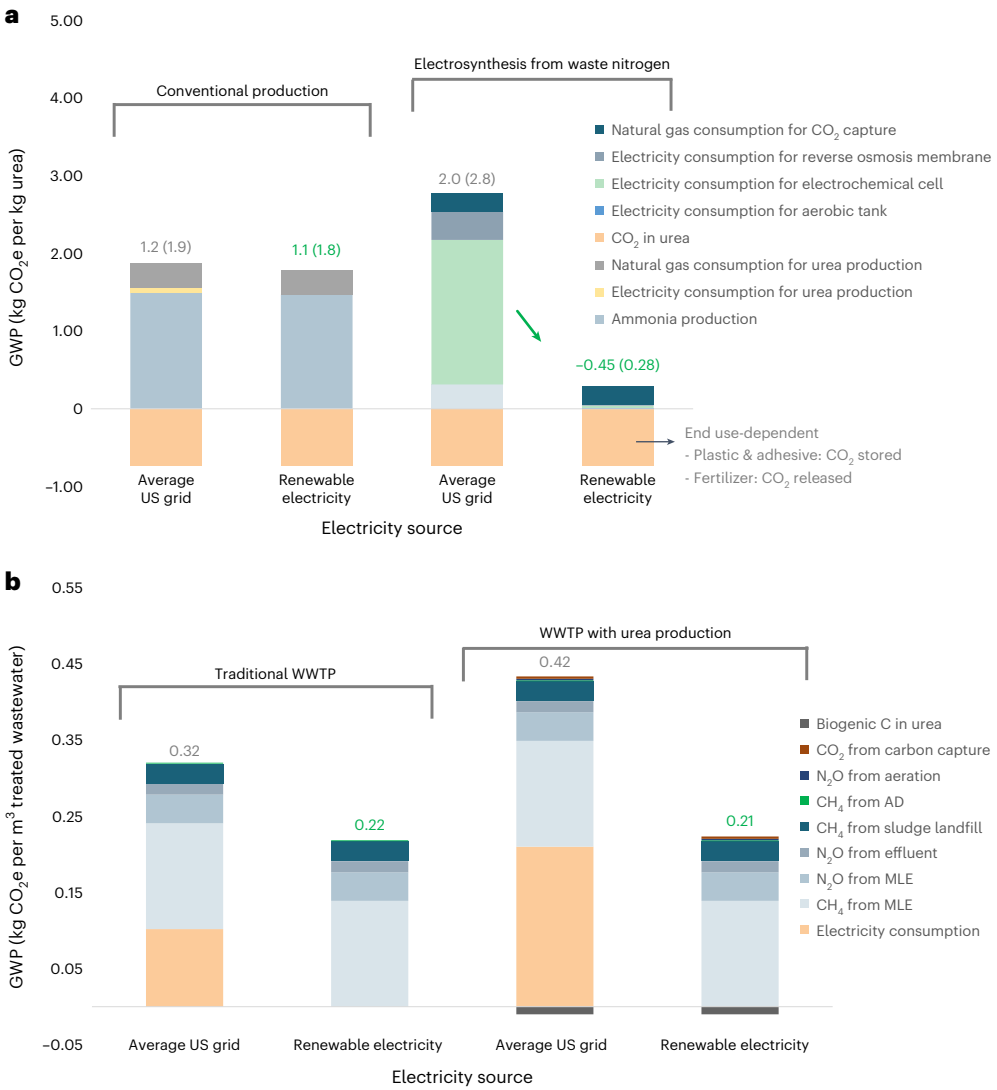

Fig. 6 | Life cycle assessment. a, Global warming potential (GWP) of urea production, conventionally or electrochemically from waste nitrogen in wastewater. The biogenic carbon content of the urea is released as CO_2 when it is used as fertilizer. It is treated in the LCA as being stored in cases when it is used as feedstock for plastics, resins and adhesives. **b**, GWP of wastewater treatment with and without electrochemical urea production. AD, anaerobic digestion; MLE, modified Ludzack–Ettinger.

electrochemical cell. The anodic potentials translate into an estimated full cell potential of 2 V when the oxidation evolution reaction (OER) is performed, but will be 1.35 V when, in the future, the reaction is paired with a lower-applied-potential anodic reaction (0.65 V lower than that of the OER). When we adopt an electricity carbon intensity of 0.12 kg CO_2e MJ^{-1}, this corresponds to reducing the GHG emission from 2 to 1.4 kg CO_2e per kg urea. When powered by renewable electricity (3 g CO_2e MJ^{-1}), the GHG emissions for conventional production are slightly reduced from 1.2 to 1.1 kg CO_2e per kg urea. This approach consumes much more natural gas than electricity, and grid decarbonization does not appreciably reduce its GHG emissions.

The life-cycle GHG emissions of urea produced by electrochemical or conventional paths are calculated by considering the fate of the biogenic carbon contained. When urea is used in applications in which the embodied CO_2 is retained in a material for the long term (for example, in plastics), the life-cycle GHG emission for electrochemically produced urea (Fig. 6a) is −0.45 kg CO_2e kg^{-1}, compared with 1.1 kg CO_2e kg^{-1} for the conventional path. When the urea is used in agriculture as a fertilizer, where CO_2 is released in the end use, the urea's life-cycle GHG emissions are 0.28 kg CO_2e kg^{-1}, compared to 1.8 kg CO_2e kg^{-1} for the conventional path (Fig. 6a). The ideal scenario for electrochemical production of urea from nitrogen in wastewater therefore entails the use of renewable electricity and improved electrochemical technology (for example, by achieving the parameters outlined in Supplementary Table 6). We assume that natural gas provides heat to the carbon capture unit. If biogas were available to use instead, the GHG emissions from the electrochemical pathway would decrease.

Exploring product-based and treatment plant-based functional units for waste-based products is valuable[26,27], because analysts can design waste-based systems that offer environmental benefits compared to both the baseline product and waste treatment technologies. We therefore compared a baseline WWTP (Supplementary Fig. 32) with one incorporating urea electrosynthesis (Supplementary Fig. 33), using a functional unit of 1 m^3 of treated wastewater. Adding urea production to the WWTP increases the CED by 28% (Supplementary Fig. 35). The WWTP with urea production slightly increases the GHG emissions from 0.32 (baseline) to 0.42 kg CO_2e m^{-3} (Fig. 6b) when today's grid provides electricity, but the emissions decrease to 0.31 kg CO_2e m^{-3} when the facility is powered by renewable electricity (Fig. 6b).

In alignment with the electrochemistry LCA literature, our results underscore the promise of electrochemistry to decarbonize chemical production when low-cost renewable electricity becomes widely available[28]. Our results add to the urgency of calls to pursue ever-increasing levels of renewable electricity in the grid[29].

Conclusions

The hybrid catalyst studied here provides an advance in urea selectivity, achieving 75% FE in simulated wastewater containing 1,000 ppm NO_3^- [N]. Control experiments, in situ spectroscopy and calculations paint a picture where the Zn/Cu hybrid catalyst enables independent tailoring of barrier energies for each of the two steps (the first C–N bond-formation step and the protonation step from $*CO_2NH_2$ to $*COOHNH_2$), thus providing a relay catalysis path and enabling the increase in urea selectivity.

Methods

Chemicals

The KNO_3, $KHCO_3$, NH_4COONH_2 (AC), Zn nanoparticles (average size of 40–60 nm, ≥99% trace) and Cu nanoparticles (average sizes of 25 nm, TEM) were purchased from Sigma-Aldrich. $Zn_{50}Cu_{50}$ nanoparticles (average size of 40 nm, 99.9% trace) were purchased from US Research Nanomaterials. Bipolar membranes were acquired from the Fuel Cell Store. The Cu target (99.999%) for electron-beam deposition was purchased from Kurt J. Lesker. Polytetrafluoroethylene (PTFE) membrane with an average pore size of 450 nm was obtained from Beijing Zhongxingweiye Instrument Co. All chemicals used in this work were used as received. The aqueous solutions were prepared using distilled water with a resistivity of 18.2 MΩ cm with a UV radiation accessory.

Gas-diffusion electrode preparation

Single-component Cu catalysts were prepared by sputtering Cu (200 nm) on PTFE fibre substrate or spray-coating Cu nanoparticle ink onto hydrophobic carbon paper (Freudenberg H23C9, Fuel Cell Store). Single-component Zn catalysts were prepared by spray-coating Zn nanoparticle ink onto a hydrophobic carbon paper. To prepare the ink, 8-mg nanoparticles (Cu or Zn) were dispersed in 2 ml of methanol, then 16 µl of Nafion (5%) was added and the ink was sonicated for 1 h. The Cu or Zn nanoparticle inks were spray-coated onto the carbon paper with a loading of ~2 mg cm^{-2} and dried in air, then stored in a glove box before electrochemical tests. The Zn/Cu hybrid catalysts were prepared by spray-coating Zn nanoparticle ink onto a sputtered or spray-coated Cu film, depending on the hybrid catalyst electrode configuration. The loading of Zn nanoparticles was controlled during spray coating. The sputtered Cu substrate was fabricated by electron-beam evaporation of a Cu target onto a hydrophobic porous PTFE fibre substrate[30] at a deposition rate of ~1 Å s^{-1} until a thickness of ~200 nm was achieved. Other mono-component and hybrid catalysts were prepared by spray-coating the corresponding nanoparticle inks on substrates, and the preparation method for these inks was the same as for the Cu and Zn inks.

Spray-coating method

The ink was prepared by mixing 10 mg of nanoparticles, 5% Nafion (20 µl for the Zn–0.5/Cu sample and 30 µl for the 3D Zn/Cu sample) and 3 ml of methanol, followed by sonication for 1 h at room temperature. The as-prepared ink was sprayed ~3 cm away from the support with a GDL at a vertical angle using N_2 gas at 1 bar. The ink emerging from the mouth of the airbrush gun was controlled to avoid wetting of the support. The spraying direction was changed frequently, back and forth. Supplementary Fig. 4 shows the uniformity of the catalyst and run-to-run reproducibility.

Preparation of the 3D Zn/Cu hybrid catalyst

First, 0.27 mg cm^{-2} of copper nanoparticle ink (weighted loading amount of a catalyst mixture of Zn/Cu and Nafion after drying) was sprayed onto hydrophobic carbon paper measuring 3 × 3 cm^2. After drying in air, Zn was further deposited in 5 mM $Zn(NO_3)_2$ aqueous solution, using sprayed carbon paper as the work electrode, under 1 mA cm^{-2} for 100 s. The sample was fully washed with water and then stored in a glove box.

Electrochemical performance

The electrochemical data were collected using an electrochemical station (Metrohm Autolab PGSTAT204) in a flow cell system, with catalysts to be measured as the cathode, a Ag/AgCl electrode as the reference electrode, and nickel foam as the counter electrode. The catholyte varied depending on the test purpose, but was 0.1 M $KHCO_3$ with 500 ppm KNO_3 [N] unless otherwise specified. The anolyte was always 1 M KOH solution. A bipolar membrane was used to separate the anolyte and catholyte. Before electrochemical measurements, the catholyte was purged with CO_2 or Ar. CO_2 gas was fed from the backside (no-catalyst side) of the gas-diffusion electrode at a flow rate of 30 s.c.c.m. To detect the gaseous products, a flow rate of 1 s.c.c.m. was used, and the tail gas was sampled after 20 min of equilibration. The tail gas composition was evaluated by gas chromatography. The catholyte and anolyte were circulated using a peristaltic pump.

The potentials (E) were converted to values versus RHE:

$$E_{RHE} = E_{Ag/AgCl} + 0.198 + 0.0591 \times pH \quad (4)$$

$$E_{RHE} = E_{SCE} + 0.24 + 0.0591 \times pH \quad (5)$$

Characterization

The morphology and elemental distributions of the samples were examined by field-emission scanning electron microscopy (SEM; 5 kV, Hitachi, SU5000). The XRD (MiniFlex600) pattern was collected with Cu Kα as the radiation source. High-resolution TEM analyses were conducted at an electron acceleration voltage of 300 kV (FET Tecnai F30). The high-resolution XPS (Thermo Fisher ECSALAB 250Xi) spectra were collected using monochromatic Al Kα X-rays, the pass energy was 20 eV, and the energy step size was 0.1 eV. The depth profile was achieved by Ar bombardment in the chamber.

In the in situ IRRAS characterization, carbon paper was used as the substrate/GDL. The hybrid catalyst was used as the cathode in electrolytes of 0.1 M $KHCO_3$ with 0.1 M KNO_3 saturated by CO_2. Pt wire was used as the anode electrode and Ag/AgCl as the reference electrode. The in situ IRRAS spectra were collected using a Nicolet IS50 spectrometer equipped with a mercury cadmium telluride (MCT) detector. For the control IRRAS experiment, Ar was purged into the solution (0.1 M $KHCO_3$ and 0.1 M KNO_3) until saturated.

In the XAS characterization, carbon paper was used as the substrate/GDL. The hybrid catalyst was used as the cathode in electrolytes of 0.1 M $KHCO_3$ with 0.1 M KNO_3 saturated by CO_2. Pt wire was used as the anode electrode, and saturated calomel electrode as the reference electrode. The XAS spectra at the Cu and Zn K-edges were recorded at the BL11B beamline of Shanghai Synchrontron Radiation Facility (SSRF). The beam current of the storage ring was 220 mA in a top-up mode. The incident photons were monochromatized by a Si(111) double-crystal monochromator, with an energy resolution of $\Delta E/E \approx 1.4 \times 10^{-4}$. The spot size at the sample was ~200 µm. All the operando XAFS spectra at the Cu and Zn K-edge were collected in a fluorescence mode with a Lytle ionization chamber filled with Ar. The K-edge of Cu foil (8,979 eV) was used for the calibration.

In the in situ SERS characterization, different conditions were used, including urea synthesis condition (1 M $KHCO_3$ + 1 M KNO_3), the AC reference condition (0.03 M AC + 0.7 M $KHCO_3$), $KHCO_3$ (1 M), K_2CO_3 (1 M) and KNO_3 (1 M). The characterization was performed on a Renishaw inVia Raman spectrometer in a modified flow cell with a water immersion objective (×63) and a 785-nm laser with 0.5% power, using

10-s integration and accumulation with four scans per region. Pt wire and Ag/AgCl were used as anode and reference electrodes, respectively.

The gas-phase products, including CO, CH_4, C_2H_4 and H_2, were tested by a gas chromatograph (GC, PerkinElmer Clarus 600) equipped with a thermal conductivity detector and a flame ionization detector. The liquid products, including $HCOO^-$, NH_4^+, C_2H_5OH, CH_3COOH and n-propanol, and CH_3NH_2 were analysed using a ^1H NMR spectrometer (Agilent DD2, 600 MHz), using a known amount of acetonitrile as an internal standard. The detection of ammonia was also achieved by ^1H NMR, where the electrolyte was acidified to reach a pH of ~3 by addition of an appropriate amount of 0.5 M H_2SO_4. In this study, the UV–vis adsorption spectroscopy was not able to detect ammonia because of interference from the CO_2RR products. An ionic detector was used to detect N_2, N_2O, NO_x and so on, by feeding Ar carrier gas with a flow rate of 1 s.s.c.m.

The product urea was quantified by multiple methods. First, the diacetylmonoxime method was carried out using UV–vis adsorption spectroscopy[31,32]. Aluminium foil was used to cover the glass bottle containing electrolyte samples before tests to avoid light illumination. The extracted electrolyte was initially subjected to the quantification of urea without any post-processing. Second, the urea was quantified by ^{14}N NMR. The isotope-labelled ^{15}N NMR results show peak positions that are different from the unlabelled ones. For the experiments in Supplementary Fig. 11, all the electrolytes were prepared using distilled water with a resistivity of 18.2 MΩ cm with a UV radiation accessory in a carefully cleaned and sealed transparent container. The container with electrolytes was then irradiated under UV light for 2 h before electrochemical tests. The tests were carried out immediately after UV irradiation. A clean electrochemical cell and accessories were used.

DFT calculations

All ab initio DFT calculations were performed by employing the projector augmented wave method as implemented in the Vienna Ab initio Simulation Package[33,34]. The generalized gradient approximation in the parametrization of Perdew–Burke–Ernzerhof[35] was implemented to describe the exchange-correlation function. A plane-wave cutoff of 450 eV and 3 × 3 × 1 gamma-centred k-point grids generated by the Monkhorst–Pack[36] scheme were used for all calculations. A charged water overlayer[37] together with the zero damping DFT-D3 method of Grimme[38] were considered to account for the field and solvation effects as well as long-range van der Waals interactions. A hexagonal charged water overlayer was added onto a 3 × 3 × 4 face-centred cubic (111) surface of Ag and Cu and 3 × 3 × 4 hexagonal close-packed (0001) surface on Zn, which includes five water molecules and a hydronium (H_3O^+). A vacuum region of more than 15-Å thickness was included along the perpendicular direction to avoid artificial interactions. All atoms in the bottommost two layers were fixed during the structural optimization, while the other atoms, as well as the adsorbates, were allowed to relax. Geometries were optimized by considering different adsorption sites on the surfaces with respect to the charged water overlayer, and those with the lowest energy from DFT calculations were reported. Ab initio molecular dynamics simulations were conducted in a constant-volume, constant-temperature ensemble and performed for 10 ps with the time step set to 0.5 fs, to optimize the structure of the charged water overlayer. The Nosé–Hoover thermostat method was used to maintain the temperature at 300 K. The atomic coordinates of the optimized models are provided in Supplementary Data 1.

Life cycle inventory

The commercial software packages GPS-X and CapdetWorks were used to generate wastewater treatment plant mass and energy flows. Electricity generation and the natural gas supply are important background systems for this analysis. We used emission factors for electricity and natural gas from the Greenhouse Regulated Emissions and Energy use in Technologies model (GREET). Data sources for other parameters, including direct CH_4 and N_2O emissions from wastewater treatment plants, are provided in Supplementary Tables 10–12.

Life cycle impact assessment

Considering the importance of the water–energy nexus and addressing climate change, we selected global warming potential and cumulative energy demand as the two impact categories for the LCA.

Data availability

All data supporting the findings of this study are available within the Article and Supplementary Information. Source data are provided with this paper.

References

1. Fowler, D. et al. The global nitrogen cycle in the twenty-first century. *Philos. Trans. R. Soc. B* **368**, 20130164 (2013).
2. Hattori, M., Iijima, S., Nakao, T., Hosono, H. & Hara, M. Solid solution for catalytic ammonia synthesis from nitrogen and hydrogen gases at 50 °C. *Nat. Commun.* **11**, 2001 (2020).
3. *Molecule of the Week Archive: Ammonia* (ACS); www.acs.org/content/acs/en/molecule-of-the-week/archive/a/ammonia.html
4. *Molecule of the Week Archive: Urea* (ACS); www.acs.org/content/acs/en/molecule-of-the-week/archive/u/urea.html
5. Lv, C. et al. Selective electrocatalytic synthesis of urea with nitrate and carbon dioxide. *Nat. Sustain.* **4**, 868–876 (2021).
6. *Ammonia Technology Roadmap* (International Energy Agency, 2021).
7. Cogert, K. I., Ziels, R. M. & Winkler, M. K. H. Reducing cost and environmental impact of wastewater treatment with denitrifying methanotrophs, anammox and mainstream anaerobic treatment. *Environ. Sci. Technol.* **53**, 12935–12944 (2019).
8. Damma, D., Ettireddy, P., Reddy, B. & Smirniotis, P. A review of low temperature NH_3-SCR for removal of NO_x. *Catalysts* **9**, 349 (2019).
9. Wu, Y., Jiang, Z., Lin, Z., Liang, Y. & Wang, H. Direct electrosynthesis of methylamine from carbon dioxide and nitrate. *Nat. Sustain.* **4**, 725–730 (2021).
10. Saravanakumar, D., Song, J., Lee, S., Hur, N. H. & Shin, W. Electrocatalytic conversion of carbon dioxide and nitrate ions to urea by a titania–Nafion composite electrode. *ChemSusChem* **10**, 3999–4003 (2017).
11. Lv, C. et al. A defect engineered electrocatalyst that promotes high-efficiency urea synthesis under ambient conditions. *ACS Nano* **16**, 8213–8222 (2022).
12. Li, J., Zhang, Y., Kuruvinashetti, K. & Kornienko, N. Construction of C–N bonds from small-molecule precursors through heterogeneous electrocatalysis. *Nat. Rev. Chem.* **6**, 303–319 (2022).
13. Jouny, M. et al. Formation of carbon–nitrogen bonds in carbon monoxide electrolysis. *Nat. Chem.* **11**, 846–851 (2019).
14. Tao, Z., Rooney, C. L., Liang, Y. & Wang, H. Accessing organonitrogen compounds via C–N coupling in electrocatalytic CO_2 reduction. *J. Am. Chem. Soc.* **143**, 19630–19642 (2021).
15. Meng, N. et al. Oxide-derived core-shell Cu@Zn nanowires for urea electrosynthesis from carbon dioxide and nitrate in water. *ACS Nano* **16**, 9095–9104 (2022).
16. Fernandez-Nava, Y., Maranon, E., Soons, J. & Castrillon, L. Denitrification of wastewater containing high nitrate and calcium concentrations. *Bioresour. Technol.* **99**, 7976–7981 (2008).
17. Moloantoa, K. M., Khetsha, Z. P., van Heerden, E., Castillo, J. C. & Cason, E. D. Nitrate water contamination from industrial activities and complete denitrification as a remediation option. *Water* **14**, 799 (2022).
18. Shi, L., Liu, L., Yang, B., Sheng, G. & Xu, T. Evaluation of industrial urea energy consumption (EC) based on life cycle assessment (LCA). *Sustainability* **12**, 3793 (2020).

19. Bargiacchi, E., Antonelli, M. & Desideri, U. A comparative assessment of power-to-fuel production pathways. *Energy* **183**, 1253–1265 (2019).
20. Shibata, M., Yoshida, K. & Furuya, N. Electrochemical synthesis of urea on reduction of carbon dioxide with nitrate and nitrite ions using Cu-loaded gas-diffusion electrode. *J. Electroanal. Chem.* **387**, 143–145 (1995).
21. Shibata, M., Yoshida, K. & Furuya, N. Electrochemical synthesis of urea at gas-diffusion electrodes—IV. Simultaneous reduction of carbon dioxide and nitrate ions with various metal catalysts. *J. Electrochem. Soc.* **145**, 2348–2353 (1998).
22. Wang, Y. et al. Enhanced nitrate-to-ammonia activity on copper-nickel alloys via tuning of intermediate adsorption. *J. Am. Chem. Soc.* **142**, 5702–5708 (2020).
23. Keuleers, R., Desseyn, H. O., Rousseau, B. & Alsenoy, C. V. Vibrational analysis of urea. *J. Phys. Chem. A* **103**, 4621–4630 (1999).
24. Manivannan, M. Investigation of inhibitive action of urea–Zn^{2+} system in the corrosion control of carbon steel in sea water. *Int. J. Eng. Sci. Technol.* **3**, 8084–8060 (2011).
25. Bossa, J. B., Theulé, P., Duvernay, F., Borget, F. & Chiavassa, T. Carbamic acid and carbamate formation in NH_3:CO_2 ices—UV irradiation versus thermal processes. *Astron. Astrophys.* **492**, 719–724 (2008).
26. Lam, K. L., Zlatanović, L. & van der Hoek, J. P. Life cycle assessment of nutrient recycling from wastewater: a critical review. *Water Res.* **173**, 115519 (2020).
27. Gowd, S. C. et al. Life cycle assessment of comparing different nutrient recovery systems from municipal wastewater: a path towards self-reliance and sustainability. *J. Clean. Prod.* **410**, 137331 (2023).
28. Xia, R., Overa, S. & Jiao, F. Emerging electrochemical processes to decarbonize the chemical industry. *JACS Au* **2**, 1054–1070 (2022).
29. *Net Zero by 2050* (International Energy Agency, 2021); https://www.iea.org/reports/net-zero-by-2050
30. Arquer, F. P. G. D. et al. CO_2 electrolysis to multicarbon products at activities greater than 1 A cm^{-2}. *Science* **367**, 661–666 (2020).
31. Rahmatullah, M. & Boyde, T. R. C. Improvements in the determination of urea using diacetylmonoxime; methods with and without deproteinization. *Clin. Chim. Acta* **107**, 3–9 (1980).
32. Chen, C. et al. Coupling N_2 and CO_2 in H_2O to synthesize urea under ambient conditions. *Nat. Chem.* **12**, 717–724 (2020).
33. Kresse, G. & Hafner, J. Ab initio molecular dynamics for liquid metals. *Phys. Rev. B* **47**, 558–561 (1993).
34. Kresse, G. & Hafner, J. Ab initio molecular-dynamics simulation of the liquid-metal–amorphous-semiconductor transition in germanium. *Phys. Rev. B* **49**, 14251–14269 (1994).
35. Perdew, J. P., Burke, K. & Ernzerhof, M. Generalized gradient approximation made simple. *Phys. Rev. Lett.* **77**, 3865–3868 (1996).
36. Monkhorst, H. J. & Pack, J. D. Special points for Brillouin-zone integrations. *Phys. Rev. B* **13**, 5188–5192 (1976).
37. Montoya, J. H., Shi, C., Chan, K. & Nørskov, J. K. Theoretical insights into a CO dimerization mechanism in CO_2 electroreduction. *J. Phys. Chem. Lett.* **6**, 2032–2037 (2015).
38. Grimme, S., Antony, J., Ehrlich, S. & Krieg, H. A consistent and accurate ab initio parametrization of density functional dispersion correction (DFT-D) for the 94 elements H-Pu. *J. Chem. Phys.* **132**, 154104 (2010).

Acknowledgements

We acknowledge the support of the Banting Postdoctoral Fellowships Program (no. 01353-000, Y.L.) and the National Science Fund of China for Distinguished Young Scholars (no. 52125309, B.L.). We thank the staff at the BL11B beamline of Shanghai Synchrotron Radiation Facility (SSRF) for their technical assistance.

Author contributions

Y.L. and K.X. proposed the idea. Y.L. contributed to all experimental work, data analysis and the paper. K.X. contributed to the catalytic performance tests of the 2D hybrid catalysts and analysis. P.O. contributed to DFT calculations, with feedback from X.-Y.L. C.L. and J.B.D. contributed to LCA analysis with Y.L., with K.X.'s feedback. T.P. contributed to in situ IRRAS experiments. Z.Z. and B.L. contributed to in situ XAS characterization. Z.C. and Y.L. performed the in situ SERS characterization and analysis. N.W. and I.G. contributed to material synthesis. D.S. contributed to the discussion of the work. E.H.S. supervised the study.

Competing interests

The authors declare no competing interests.

Additional information

Supplementary information The online version contains supplementary material available at https://doi.org/10.1038/s41929-023-01020-4.

Correspondence and requests for materials should be addressed to Jennifer B. Dunn or Edward H. Sargent.

Peer review information *Nature Catalysis* thanks Feng Jiao, Yafei Li and Heiko Keller for their contribution to the peer review of this work.